CHEMISTRY

Electrochemical synthesis of nitric acid from air and ammonia through waste utilization

Yuting Wang[1], Yifu Yu[1,*], Ranran Jia[1], Chao Zhang[1] and Bin Zhang [ID][1,2,*]

ABSTRACT

Commercial nitric acid (HNO_3) and ammonia (NH_3) are mostly produced through the Ostwald process and the Haber-Bosch process, respectively. However, high energy demand and enormous greenhouse gas accompy these processes. The development of economical and green ways to synthesize HNO_3 and NH_3 is highly desirable for solving the global energy and environmental crisis. Here, we present two energy-efficient and environmentally friendly strategies to synthesize HNO_3 and NH_3 at distributed sources, including the electrocatalytic oxidation of N_2 in air to HNO_3 and the electrocatalytic reduction of residual NO_3^- contamination in water to NH_3. The isotope-labeling studies combined with theoretical calculation reveal the reaction path of the two proposed strategies, confirming the origin of the electrochemical products. Importantly, the electrooxidation-generated NO_3^- ions may also serve as reactants for the electroreduction synthesis of NH_3 in the future. Our work may open avenues for energy-efficient and green production of HNO_3 and NH_3 at distributed sources.

Keywords: ammonia, nitric acid, distributed sources, electrocatalysis, green synthesis

INTRODUCTION

Transformations of nitrogen into reactive forms, particularly nitric acid (HNO_3) and ammonia (NH_3), are vital to living organisms and industrial processes [1–4]. The worldwide production of HNO_3 and NH_3 was 50 and 150 million metric tons, respectively, in 2017 [5]. Commercial HNO_3 is produced through the catalytic oxidation of NH_3 (Ostwald process), but this approach is energy-intensive [5]. On the other hand, NH_3 is mostly manufactured using the Haber-Bosch method [6–9], which consumes $\sim$2% of global power and discharges $\sim$1.5% of global greenhouse gas [10–16]. Moreover, the large-scale chemical plants, and hence centralized HNO_3 and NH_3 sources, induce a serious waste of fossil fuels during the transportation process [17]. Therefore, searching novel solutions that allow energy-efficient and environmentally friendly synthesis of HNO_3 and NH_3 at distributed sources are urgently needed [18,19]. Electrocatalysis represents a potentially alternative strategy [20]. However, present electrocatalysis is focused on preparing NH_3 through the reduction of pure dinitrogen, which is produced by the energy-intensive air-separation process [21–24]. Thus, it is of great interest to develop novel electrochemical routes to achieving green synthesis of HNO_3 and NH_3 under benign conditions.

Herein, we present two electrochemical strategies. Strategy I is the electrocatalytic oxidation of N_2 to HNO_3 by using air as the nitrogen source. Strategy II is the electrochemical reduction preparation of $NH_{3(aq)}$ from residual nitrate ion (NO_3^-) contamination in water [25,26]:

$$NO_3^-{}_{(aq)} + 6H_2O_{(liq)} + 8e^- \rightarrow NH_{3(aq)} + 9OH^-_{(aq)}. \tag{1}$$
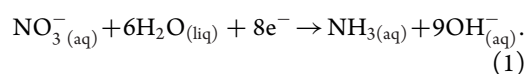
We found that N_2 is electro-oxidized into HNO_3 over platinum foil with $\sim$1.23% Faradaic efficiency at +2.19 V vs. RHE (the reversible hydrogen electrode) and the waste of NO_3^- is electro-reduced with approximately 33.6% $NH_{3(aq)}$ selectivity at −0.65 V vs. RHE over Co_3O_4 nanorod arrays. Our results demonstrate how the electrochemical methods of Strategy I and Strategy II produce HNO_3 and NH_3 at distributed sources. These findings provide a new avenue for producing the reactive nitrogen species

[1]Department of Chemistry, Institute of Molecular Plus, School of Science, Tianjin University, Tianjin 300072, China and [2]Collaborative Innovation Center of Chemical Science and Engineering, Tianjin 300072, China

*Corresponding authors. E-mails: bzhang@tju.edu.cn; yyu@tju.edu.cn

in an 'economic' and 'clean' way, especially once the electrocatalysis reaction is driven by renewable energy [27].

RESULTS AND DISCUSSION

An H-type cell divided by a proton-exchange membrane was used for the electrocatalytic tests of Strategy I (Fig. 1a). To explore the catalytic behavior of N_2 electrooxidation (Strategy I), air was bubbled onto the anode. H_2O in electrolyte (0.3 M K_2SO_4) and N_2 in air combine with platinum foil as an electrocatalyst to form HNO_3. We tested the linear sweep voltammetry curves of platinum foil in

Ar- and air-saturated electrolyte under ambient conditions (Fig. 1b). All potentials in this work were recorded and converted to the RHE scale. As the potential moves above +2.13 V, the current density is distinguishably enhanced under air-saturated electrolyte, revealing that N_2 in air can be catalysed into oxidative products. The produced NO_3^- and NO_2^- are quantified based on the standard method [28] by using ultraviolet-visible (UV-Vis) spectrophotometry (Supplementary Fig. S1, available as Supplementary Data at *NSR* online). Anion chromatography was also adopted to confirm the accuracy of UV-Vis spectrophotometry for detecting the yield of NO_3^- (Supplementary Table S1, available as
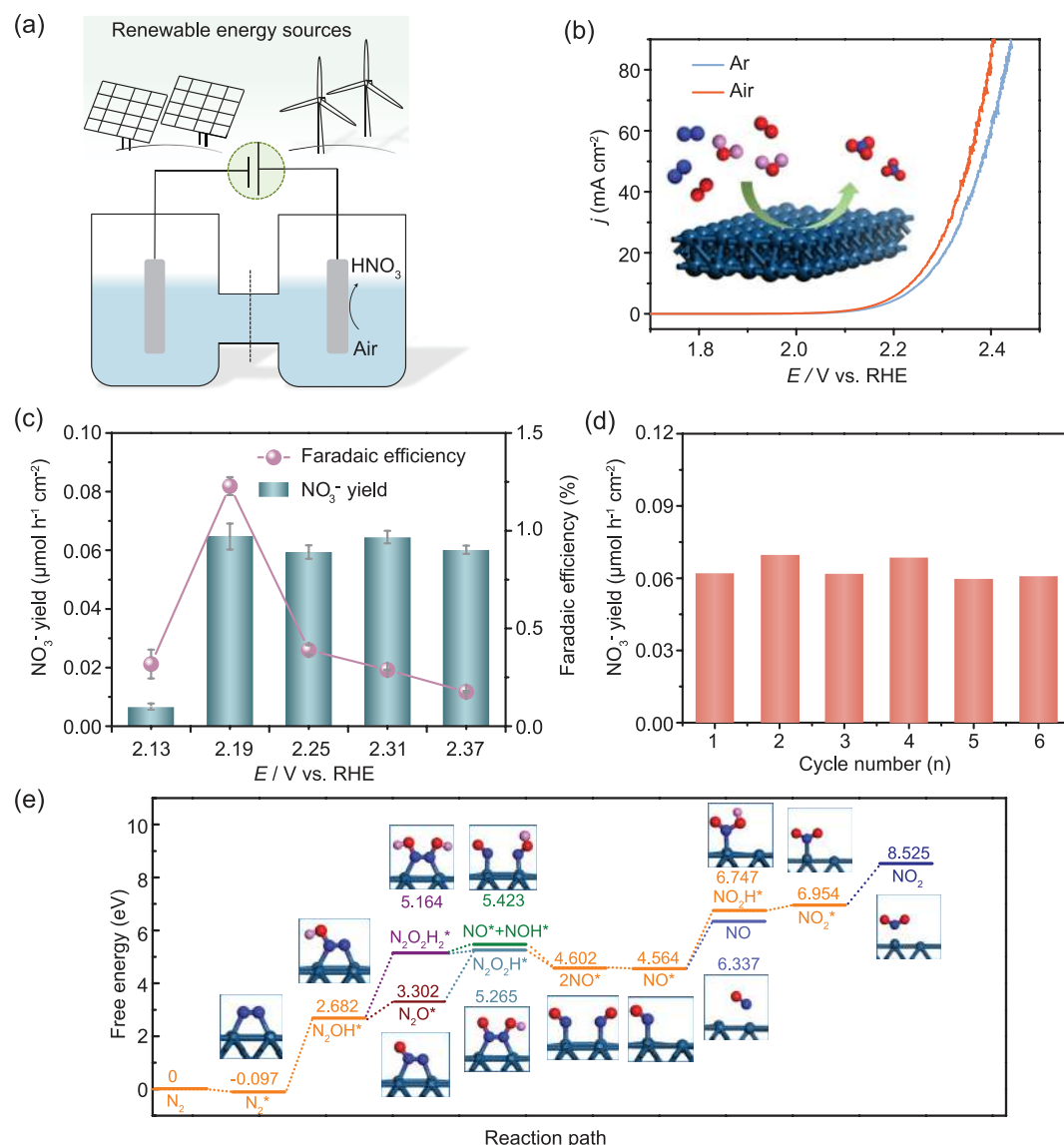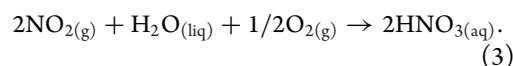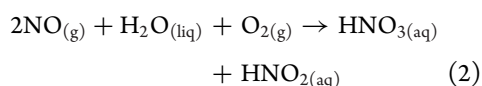

Figure 1. (a) Schematic illustration for as-proposed Strategy I. (b) Linear sweep voltammetric curves of platinum foil in Ar-saturated (blue line) and air-saturated (red line) electrolyte. (c) Yields of NO_3^- and Faradaic efficiencies after potentiostatic test at given potentials. (d) The cycling tests of N_2 electrooxidation over the same piece of Pt electrode. (e) Calculated free-energy diagram for N_2 electrooxidation over platinum foil. Ball-and-stick model in (b) and (e): blue ball (N atom), red ball (O atom), pink ball (H atom) and green ball (Pt atom).

Supplementary Data at *NSR* online). The effect of the anode potentials on the yields of oxidative products and the corresponding Faradaic efficiencies were investigated (Fig. 1c). Although the gap in the current density between Ar and air condition keeps enlarging with the increase in potential, the highest Faradaic efficiency of 1.23% for NO_3^- was obtained at +2.19 V. The yields of NO_3^- and NO_2^- at +2.19 V achieve 0.06 and 0.0004 μmol h^{-1} cm^{-2}, respectively, and remained almost unchanged with the increase in potential (Fig. 1c and Supplementary Fig. S2, available as Supplementary Data at *NSR* online). So, the optimal operating potential for N_2 electrooxidation over platinum electrocatalyst in this work was +2.19 V. Furthermore, some control experiments, including Ar-saturated electrolyte with a potentiostatic test (+2.19 V) and air-saturated electrolyte without external potential, were performed. Undetected oxidative products in both cases further confirmed the electrocatalytic oxidation of N_2 in air to NO_3^- and NO_2^- as designed in Strategy I (Supplementary Table S2, available as Supplementary Data at *NSR* online). For practical application, the durability of the catalyst is crucial. After consecutive recycling tests, the catalytic performance showed no obvious decline, demonstrating the high stability of platinum foil toward the electrooxidation of N_2 (Fig. 1d). As shown in Fig. 1e, Strategy I goes through multiple processes. We calculated the free energy of N_2 electrooxidation over the Pt (200) plane based on the X-ray diffraction (XRD) result (Supplementary Fig. S3, available as Supplementary Data at *NSR* online). First, the N_2 molecule was chemically absorbed by the platinum to form N_2^* with a total energy change of −0.097 eV, indicating that this reaction can take place spontaneously. N_2^* reacted with OH^- to produce N_2OH^* and then N_2OH^* was dehydrogenated to N_2O^* or continued to react with OH^- to produce $N_2O_2H_2^*$ with a larger reaction energy. Both N_2O^* and $N_2O_2H_2^*$ will evolve into NO^* with the intermediate of $N_2O_2H^*$ and NOH^*. Note that NO^* could be directly desorbed from the catalyst surface and then oxidized into HNO_3 and HNO_2 in solution (Equation (2)). Meanwhile, NO^* can be oxidized to NO_2^* with the intermediate of NO_2H^*. With further increase in potential, NO_2^* desorbed from the catalyst surface. Finally, NO_2 was transformed to HNO_3 in solution through Equation (3). Based on these results, we can deduce the reaction path from N_2 in air to HNO_3 via the as-proposed Strategy I:

$$2NO_{(g)} + H_2O_{(liq)} + O_{2(g)} \rightarrow HNO_{3(aq)}$$
$$+ HNO_{2(aq)} \quad (2)$$

$$2NO_{2(g)} + H_2O_{(liq)} + 1/2O_{2(g)} \rightarrow 2HNO_{3(aq)}. \quad (3)$$

To demonstrate Strategy II, involving electroreducing residual NO_3^- contamination in water, KNO_3 was added to a cathode cell and reduced into $NH_{3(aq)}$ (Fig. 2a). Presently, the main sources of nitrate for the as-proposed Strategy II are residual contamination in water, including industrial wastewater, domestic sewage, animal waste and nitrogen fertilizers. In the future, if the efficiency of Strategy I can be further improved, the electrooxidation generation of NO_3^- may also serve as a reactant for Strategy II. We constructed Co_3O_4 nanorod arrays supported on Ti mesh as a model electrocatalyst (Supplementary Fig. S4, available as Supplementary Data at *NSR* online). The linear sweep voltammetry curves of the Co_3O_4 electrode in 0.1 M K_2SO_4 electrolyte with and without KNO_3 were performed under ambient conditions (Fig. 2b). The current density was obviously enhanced in the presence of KNO_3, indicating that NO_3^- in solution can be catalysed into reductive products. The yields of $NH_{3(aq)}$ [28] and NO_2^- were quantified based on UV-Vis spectrophotometers (Supplementary Fig. S5, available as Supplementary Data at *NSR* online). The cation chromatography method was also adopted to confirm the accuracy of UV-Vis spectrophotometry for detecting the yield of $NH_{3(aq)}$ (Supplementary Table S3, available as Supplementary Data at *NSR* online). Following the potentiostatic test conducted at −0.65 V vs. RHE, which corresponded to 100 mA cm^{-2} of current density (Fig. 2b), the selectivity of different reductive products is displayed in Fig. 2c. The selectivity of $NH_{3(aq)}$ was 33.6% over the Co_3O_4 electrode, and the other reductive products included NO_2^-, NO_x, N_2 and N_2H_4, etc. [29–31]. Furthermore, the Co_3O_4 electrode supported on the Ti substrate was conducted under a potentiostatic test (−0.65 V) in 0.1 M K_2SO_4 electrolyte without KNO_3. The negligible $NH_{3(aq)}$ in the final solution further confirms the electrocatalytic reduction of NO_3^- to $NH_{3(aq)}$ via Strategy II (Supplementary Fig. S6, available as Supplementary Data at *NSR* online). The bare Ti substrate showed a much smaller yield of $NH_{3(aq)}$ (0.029 mmol h^{-1} cm^{-2}) compared to that of Co_3O_4 supported on the Ti substrate (0.854 mmol h^{-1} cm^{-2}), indicating the high activity of Co_3O_4 for the electrocatalytic reduction of NO_3^- (Supplementary Fig. S6, available as Supplementary Data at *NSR* online). During the consecutive recycling test, the catalytic activities displayed almost no decline (Fig. 2d). And the Co_3O_4 electrode was maintained well after the electroreduction test (Supplementary Fig. S7, available as Supplementary Data at *NSR* online).
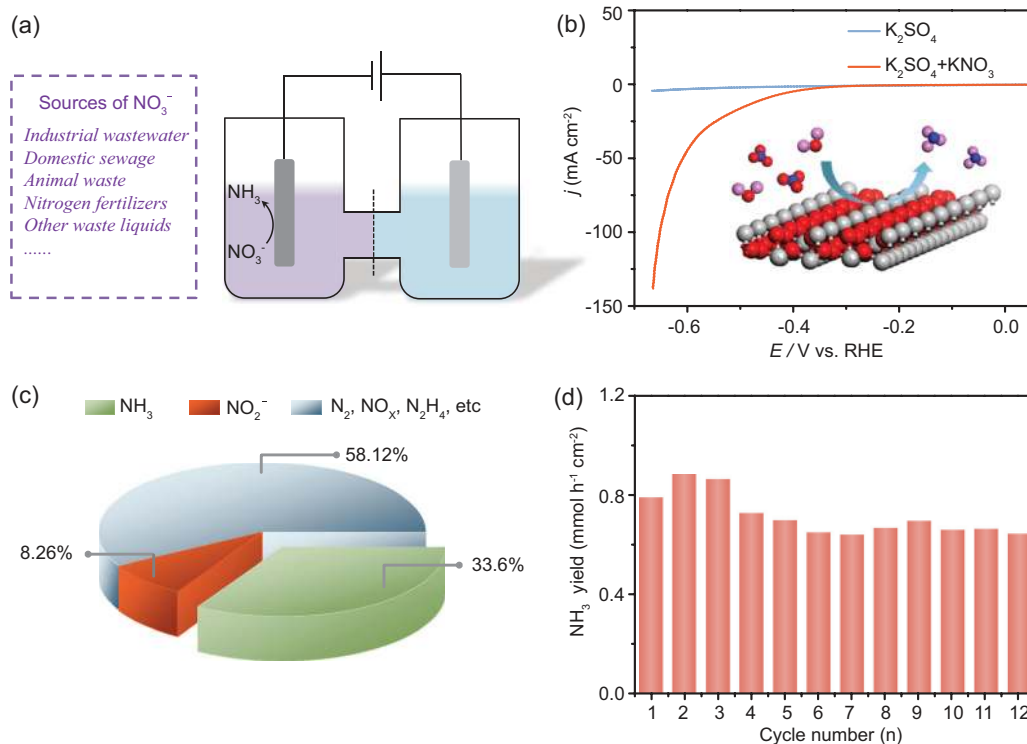
Figure 2. (a) Schematic illustration for as-proposed Strategy II. (b) Linear sweep voltammetric curves of Co_3O_4 electrode in 0.1 M K_2SO_4 electrolyte with and without KNO_3. (c) Selectivity of NO_3^- electroreduction products at −0.65 V vs. RHE. (d) The cycling tests of NO_3^- reduction over the same piece of Co_3O_4 electrode.

These results demonstrate the high durability of the Co_3O_4 electrode for NO_3^- electroreduction. Note that the electroreduction of NO_3^- was reported in previous work, but they focused on the degradation of residual NO_3^- in water into environmentally friendly products [32–34]. We herein propose utilization of the waste of NO_3^-, provided by environmental contaminations, to produce the high value-added $NH_{3(aq)}$ via electroreduction.

To confirm the origin of the NO_3^- generated from N_2 electrooxidation, we designed an isotopic-labeling study using $^{15}N_2$ (>99 atom% ^{15}N) and $^{14}N_2$ (with the natural abundance of 0.36 atom% ^{15}N) as the feeding gas for Strategy I [35]. As seen in Fig. 3a, the sample using $^{14}N_2$ as the feeding gas produced 0.44% $^{15}NO_3^-$, while the isotopic-labeled sample showed 17.40% abundance of $^{15}NO_3^-$— much higher than the natural abundance of ^{15}N. The concentration difference of ^{15}N for the isotopic-labeled sample between the $^{15}N_2$ reactant and the $^{15}NO_3^-$ product may arise from the leaking and/or residue of air in the reactor. These results clearly confirm that the N element of the generated NO_3^- via Strategy I came from N_2. We also performed an isotopic-labeling study using $K^{15}NO_3$ (20.3 atom% ^{15}N) and $K^{14}NO_3$ (0.36 atom% ^{15}N) as the reac-

tants to explore the origin of the $NH_{3(aq)}$. It can be seen that the isotopic-labeled sample exhibited 18.98% $^{15}NH_{3(aq)}$ but the sample using $K^{14}NO_3$ without an isotopic label as a reference showed only 0.36% $^{15}NH_{3(aq)}$ (Fig. 3b). These results demonstrate that the N element of the formed $NH_{3(aq)}$ via Strategy II originated from the NO_3^- species.

CONCLUSIONS

In summary, we present two energy-efficient and environmentally friendly strategies to prepare HNO_3 and NH_3 at distributed sources. Strategy I is the electrocatalytic oxidation of N_2 in air to HNO_3 and platinum foil is adopted as the model catalyst, showing a generation rate of 0.06 $\mu mol\, h^{-1}\, cm^{-2}$ for HNO_3 at +2.19 V. Strategy II is the electrocatalytic reduction of residual NO_3^- contamination in water to $NH_{3(aq)}$ and Co_3O_4 nanorod arrays supported on a Ti mesh, exhibiting a selectivity of 33.6% for $NH_{3(aq)}$ at −0.65 V. Combined with the theoretical calculation, the reaction path from N_2 in air to HNO_3 via the as-proposed Strategy I was deduced. The isotope-labeling studies using $^{15}N_2$ and $K^{15}NO_3$ confirmed the origin of the electrochemical products.
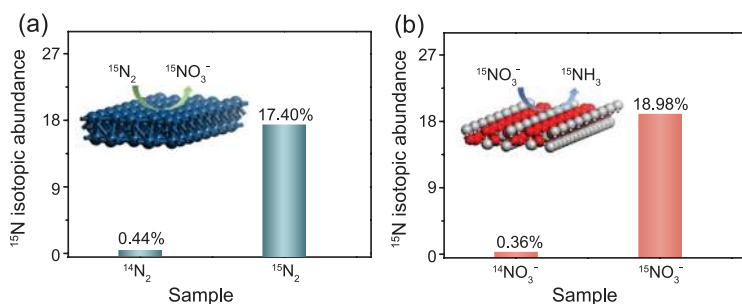
Figure 3. (a) The isotopic mass spectrometry of $^{15}NO_3^-$ with $^{15}N_2$ and $^{14}N_2$ as the feeding gas for Strategy I. (b) The isotopic mass spectrometry of $^{15}NH_{3(aq)}$ with $^{15}KNO_3$ and $^{14}KNO_3$ as the reactants for Strategy II.

Moreover, the platinum electrode and Co_3O_4 electrode showed high durability for the electrocatalytic oxidation of N_2 and the electrocatalytic reduction of NO_3^-, respectively. In the future, NO_3^- from Strategy I may also serve as a reactant for the electroreduction synthesis of NH_3. Our results presented here provide new avenues for energy-efficient and green production of HNO_3 and NH_3 at distributed sources.

METHODS

Preparation of Co_3O_4 cathode for NO_3^- reduction via Strategy II

In a typical process, 2 mmol $Co(NO_3)_2 \cdot 6H_2O$, 10 mmol urea and 8 mmol NH_4F were dissolved in 36 mL distilled water under stirring for 5 min. The aqueous solution was moved to a 50-mL Teflon-lined autoclave and then a piece of Ti mesh (1×3 cm^2) was immersed in the above solution. The autoclave was sealed and heated at 120°C for 9 h, followed by cooling down to ambient temperature. The sample was washed using distilled water and ethanol six times and then dried in a vacuum oven overnight. The dried sample was annealed at 300°C for 2 h in air to acquire the final product of Co_3O_4 nanorod arrays supported on a Ti mesh.

Characterization

The scanning electron microscopy images were acquired from a Hitachi S-4800 scanning electron microscope. Transmission electron microscopy and high-resolution transmission electron microscopy images were taken using a JEOL-2100F system. The XRD was measured using a Bruker D8 Focus Diffraction System with a Cu Kα source ($\lambda = 0.154178$ nm). X-ray photoelectron spectrum analysis was recorded via a PHI 5000 Versaprobe system using monochromatic

Al Kα radiation. All binding energies were revised according to the C 1-s peak at 284.8 eV. The ultraviolet-visible (UV-Vis) absorbance spectra were measured on a Beijing Purkinje General T6 new century spectrophotometer. Anion chromatography was performed on an ICS-1100, Thermo. Cation chromatography was conducted on an ICS-900, Thermo. The concentration of ^{15}N isotope labeling was established by isotopic mass spectrometry (MAT-271). The pH values of the electrolytes were determined using a pH-meter (LE438 pH electrode, Mettler Toledo, USA).

Electrochemical measurements

Electrochemical measurements were conducted using an electrochemical workstation (CHI 660D, Chenhua, Shanghai). A typical H-type electrolytic cell divided by a proton-exchange membrane (Nafion 117) was used. Except for special instructions, all potentials were recorded against the RHE. The potentials against the saturated calomel electrode (SCE) were translated to those against the RHE using the following equation: E (vs. RHE) $= E$ (vs. SCE) $+ 0.2415 + 0.059 \times$ pH. All the polarization curves were the steady lines after many cycles and the current density was normalized to the geometric surface area.

For the electrooxidation of N_2 to HNO_3 via Strategy I, Pt plates (1×1 cm^2) were used as both the working electrode and the counter electrode, the reference electrode was SCE and 0.3 M K_2SO_4 solution (70 mL) was adopted as the electrolyte. Air (99.99% purity) was bubbled into the anodic compartment with a flow rate of 10 mL min^{-1} in the whole electrochemical process. The linear sweep voltammetry was performed at a rate of 10 mV s^{-1} and the potentiostatic test was tested at a different anodic voltage for 20 h with the electrolyte agitated at a stirring rate of $\sim$350 rpm. An absorption flask containing 5 mL K_2SO_4 solution (0.3 M) was connected to the gas outlet of an anodic half cell to avoid the loss of products due to air bubbling. After the electrooxidation measurements, the components of the mixed solutions in the anodic compartment and absorption flask were both analysed. For comparison, the electrooxidation measurements were also measured with all the testing conditions consistent with aforementioned N_2 oxidation except that air was replaced by Ar or the external potential was removed.

The electroreduction of NO_3^- to NH_3 via Strategy II was carried out in a three-electrode configuration with as-prepared Co_3O_4 (1×1 cm^2) electrode, SCE and platinum foil as working

electrode, reference electrode and counter electrode, respectively; 0.1 M K_2SO_4 solution (80 mL) was used as the electrolyte and evenly distributed to the cathode and anode compartment. KNO_3 (100 g L^{-1}) was added into the cathode compartment as a reactant. Prior to the NO_3^- electroreduction test, the cathode electrolyte was purged with Ar (99.99% purity) for 30 min. The linear sweep voltammetry was performed at a rate of 20 mV s^{-1} and the potentiostatic test was conducted at −0.65 V for 3 h at a stirring rate of ∼350 rpm. For comparison, the electroreduction measurements were also conducted with all the testing conditions consistent with the aforementioned NO_3^- reduction except that the Co_3O_4 cathode was replaced by the Ti mesh or the Co_3O_4 cathode was immersed in electrolyte (0.1 M K_2SO_4) without the addition of KNO_3.

Ion-concentration detection methods

The electrolytes pre and post test were first diluted to appropriate concentration and then tested using a UV-Vis spectrophotometer to quantify the concentration. The concentrations of nitrate-N, nitrite-N and ammonia-N were estimated by UV-Vis spectrophotometry according to the standard method. The specific approaches are as follows.

Determination of nitrate-N
First, a certain amount of electrolyte was taken out of the electrolytic cell and diluted to 5 mL to the detection range. Then, 0.1 mL 1 M HCl and 0.01 mL 0.8 wt% sulfamic acid solution were added to the aforementioned solution. The absorption spectrum was tested using an ultraviolet-visible spectrophotometer and the absorption intensities at wavelengths of 220 and 275 nm were recorded. The final absorbance value was calculated using the equation: $A = A_{220nm} - 2A_{275nm}$. The concentration–absorbance curve was made using a series of standard potassium nitrate solutions and the potassium nitrate crystal was dried at 105–110°C for 2 h in advance.

Determination of nitrite-N
A mixture of *p*-aminobenzenesulfonamide (4 g), *N*-(1-Naphthyl)ethylenediamine dihydrochloride (0.2 g), ultrapure water (50 mL) and phosphoric acid (10 mL, $\rho = 1.70$ g/mL) was used as a color reagent. A certain amount of electrolyte was taken from the electrolytic cell and diluted to 5 mL to the detection range. Next, 0.1 mL color reagent was added into the aforementioned 5-mL solution and mixed to uniformity, and the absorption intensity at

a wavelength of 540 nm was recorded after sitting for 20 min. The concentration–absorbance curve was calibrated using a series of standard sodium nitrite solutions.

Determination of ammonia-N
Ammonia-N was determined using Nessler's reagent as the color reagent. First, a certain amount of electrolyte was taken from the electrolytic cell and diluted to 5 mL to the detection range. Next, 0.1 mL potassium sodium tartrate solution ($\rho = 500$ g/L) was added and mixed thoroughly, then 0.1 mL Nessler's reagent was put into the solution. The absorption intensity at a wavelength of 420 nm was recorded after sitting for 20 min. The concentration–absorbance curve was made using a series of standard ammonium chloride solutions and the ammonium chloride crystal was dried at 105°C for 2 h in advance.

The calibration curves of nitrate-N and nitrite-N for the electrooxidation of N_2 are shown in Supplementary Fig. S1, available as Supplementary Data at *NSR* online (0.3 M K_2SO_4 as the background solution). The calibration curves of nitrate-N, nitrite-N and ammonia-N for the electroreduction of NO_3^- are shown in Supplementary Fig. S5, available as Supplementary Data at *NSR* online (ultrapure water as the background solution).

All the results obtained using UV-Vis spectrophotometry were compared with those of ion chromatography (Supplementary Tables S1 and S3, available as Supplementary Data at *NSR* online). The pre-treatment of the cation chromatography measurement of ammonia-N after the electroreduction test was as follows. First, the electrolyte was put into a round flask and then the pH was adjusted to ∼8 by the addition of NaOH. The solution was then heated to ∼100°C and went through condensation until the 90% electrolyte was distilled. The distilled solution was collected using 35 mL ultrapure water and used for the cation chromatography measurement.

Calculation of the yield, selectivity and Faradaic efficiency

For the N_2 electrooxidation experiments via Strategy I, the yield of NO_3^- and NO_2^- was calculated using Equation (4) and Equation (5), respectively:

$$\text{Yield}_{NO_3^-} = (c_{NO_3^-} \times V)/(M_{NO_3^-} \times t \times S) \tag{4}$$

$$\text{Yield}_{NO_2^-} = (c_{NO_2^-} \times V)/(M_{NO_2^-} \times t \times S). \tag{5}$$

The Faradaic efficiency was calculated according to the charge consumed for synthesizing the NO gas

and the total charge passed through the electrode using Equation (6):

$$\text{Faradaic efficiency} = (2F \times c_{\text{NO}_3^-} \times V) / (M_{\text{NO}_3^-} \times Q), \quad (6)$$

where c_{NO3}^- is the concentration of NO_x^-, V is the volume of the electrolyte in the anode compartment, M_{NO3}^- is the molar mass of NO_3^-, M_{NO2}^- is the molar mass of NO_2^-, t is the electrolysis time, S is the geometric area of the Pt plate, F is the Faradaic constant (96 485 C mol^{-1}) and Q is the total charge passing the electrode. (Note that NO and NO_2 gas consumed two and four electrons, respectively. We prudently chose NO gas as the product to calculate the Faradaic efficiency.)

For the NO_3^- electroreduction experiments via Strategy II, the yield of $\text{NH}_{3(\text{aq})}$ was calculated using Equation (7):

$$\text{Yield}_{\text{NO}_3^-} = (c_{\text{NH}_3} \times V)/(M_{\text{NH}_3} \times t \times S). \quad (7)$$

The conversion of NO_3^- was obtained from Equation (8):

$$\text{Conversion} = \Delta c_{\text{NO}_3^-}/c_0 \times 100\%. \quad (8)$$

The selectivity of product was acquired by Equation (9):

$$\text{Selectivity} = c/\Delta c_{\text{NO}_3^-} \times 100\%, \quad (9)$$

where c_{NH3} is the concentration of $\text{NH}_{3(\text{aq})}$, Δc_{NO3}^- is the concentration difference of NO_3^- before and after electrolysis, c_0 is the initial concentration of NO_3^-, and c is the concentration of products, including $\text{NH}_{3(\text{aq})}$, NO_2^-.

^{15}N isotope-labeling experiment

The isotope-labeling reactants of $^{15}\text{N}_2$ (>99 atom% ^{15}N) and K$^{15}\text{NO}_3$ (20.3 atom% ^{15}N) were purchased from the Shanghai Research Institute of Chemical Industry Co. Ltd. The isotope-labeling concentration of products via both Strategy I and Strategy II was established by isotopic mass spectrometry from the Shanghai Engineering Research Center of Stable Isotope.

For isotope labeling the N_2 electrooxidation, we carried out the batch experiments using $^{15}\text{N}_2$ as the feeding gas for five successive times and collected all the electrolytes together after electrolysis. In order to increase the concentration of $^{15}\text{NO}_3^-$ for isotopic mass spectrometry, the collected electrolytes were first alkalified to pH ~7 by adding 1 M KOH

solution and then concentrated by 10 times via distilling at 70°C. For comparison, $^{14}\text{N}_2$ with natural-abundance ^{15}N (0.36 atom%) was used as a feeding gas to replace $^{15}\text{N}_2$ with other conditions being consistent.

For isotope labeling the NO_3^- electroreduction, the pH of final electrolyte was adjusted to ~3 using 1 M HCl solution before isotopic mass spectrometry. For comparison, K$^{14}\text{NO}_3$ with natural-abundance ^{15}N (0.36 atom%) was used as the reactant to replace K$^{15}\text{NO}_3$ with the other conditions being consistent.

Theoretical simulation

Although the XRD pattern of platinum after the electrooxidation process (not shown here) showed no obvious new species, the high oxidation state of PtOH or PtO_x might exist in an amorphous state. Considering the complexity of the electrochemical oxidation process, herein, we only adopted Pt as a model for simulation. The theoretical calculations were conducted using density functional theory with the Perdew–Burke–Ernzerbof form of generalized gradient approximation functional [36]. The plane wave energy was cut off at 400 eV. The Vienna *ab initio* simulation package was used [37,38]. The Fermi scheme was used for electron occupancy with an energy smearing of 0.1 eV. The first Brillouin zone was adopted in the Monkhorst−Pack grid [39]. The 3 × 3 × 1 k-point mesh was taken for the surface calculation. The energy of 1.0×10^{-6} eV atom^{-1} and force of 0.01 eV Å^{-1} were set as the convergence criterion for geometry optimization. The spin polarization was considered in all calculations. To accurately describe the van der Waals (vdW) interaction, the non-local van der Waals density functional (vdW-DF) was employed in our work [40,41].

The Pt (200) surface was obtained by cutting the Pt bulk along the {200} direction based on the XRD result (Supplementary Fig. S3, available as Supplementary Data at *NSR* online). The thickness of the surface slab was chosen to be a three-layer slab. In all structural optimization calculations, the bottom atoms were frozen, while the other atoms were allowed to relax. A vacuum layer as large as 15 Å was used along the c direction normal to the surface to avoid periodic interactions. For the nitrogen oxidation reaction, the reaction energies of the elementary reactions were employed to estimate the activity of the catalyst.

The free-energy changes of the nitrogen oxidation were calculated to show the reaction trend. The change in free energy (ΔG) of the per reaction step

from the initial state to the final state of the reaction was calculated as:

$$\Delta G = \Delta E + \Delta ZPE - T\Delta S,$$

where ΔE is the change in the total reaction energy obtained from the density functional theory (DFT) calculations and ΔZPE is the change in the zero-point energy. T is the temperature (298.15 K) and ΔS is the change in entropy. The free energy of H^+ is equal to that of half H_2 according to the computational hydrogen electrode model proposed by Nørskov [42], while the OH^- is estimated by $H_2O \rightarrow OH^- + H^+$. The zero-point energy and the entropies of the adsorbed nitrogen oxidation species were taken from the vibrational frequencies.

SUPPLEMENTARY DATA

Supplementary data are available at *NSR* online.

ACKNOWLEDGEMENTS

FUNDING

REFERENCES

1. Hoffman BM, Lukoyanov D and Yang ZY *et al.* Mechanism of nitrogen fixation by nitrogenase: the next stage. *Chem Rev* 2014; **114**: 4041–62.

2. Falkowski PG, Fenchel T and Delong EF. The microbial engines that drive Earth's biogeochemical cycles. *Science* 2008; **320**: 1034–9.

3. Chirik PJ. Nitrogen fixation: one electron at a time. *Nat Chem* 2009; **1**: 520–2.

4. Li L, Wang Y and Vanka S *et al.* Nitrogen photofixation over III-nitride nanowires assisted by ruthenium clusters of low atomicity. *Angew Chem Int Ed* 2017; **56**: 8701–5.

5. Chen JG, Crooks RM and Seefeldt LC *et al.* Beyond fossil fuel-driven nitrogen transformations. *Science* 2018; **360**: eaar6611.

6. Honkala K, Hellman A and Remediakis IN *et al.* Ammonia synthesis from first-principles calculations. *Science* 2005; **307**: 555–8.

7. Smil V. Detonator of the population explosion. *Nature* 1999; **400**: 415.

8. Huang P, Liu W and He Z *et al.* Single atom accelerates ammonia photosynthesis. *Sci China Chem* 2018; **61**: 1187–96.

9. Wang X, Wang W and Qiao M *et al.* Atomically dispersed Au₁ catalyst towards efficient electrochemical synthesis of ammonia. *Sci Bull* 2018; **63**: 1246–53.

10. Kitano M, Inoue Y and Yamazaki Y *et al.* Ammonia synthesis using a stable electride as an electron donor and reversible hydrogen store. *Nat Chem* 2012; **4**: 934–40.

11. Smith BE. Nitrogenase reveals its inner secrets. *Science* 2002; **297**: 1654–5.

12. van Kessel MA, Speth DR and Albertsen M *et al.* Complete nitrification by a single microorganism. *Nature* 2015; **528**: 555–9.

13. Wang L, Xia M and Wang H *et al.* Greening ammonia toward the solar ammonia refinery. *Joule* 2018; **2**: 1055–74.

14. Smil V. *Enriching the Earth: Fritz Haber, Carl Bosch, and the Transformation of World Food Production.* Cambridge, MA: MIT Press, 2004.

15. Li H, Shang J and Ai Z *et al.* Efficient visible light nitrogen fixation with BiOBr nanosheets of oxygen vacancies on the exposed {001} facets. *J Am Chem Soc* 2015; **137**: 6393–9.

16. Qiu W, Xie XY and Qiu J *et al.* High-performance artificial nitrogen fixation at ambient conditions using a metal-free electrocatalyst. *Nat Commun* 2018; **9**: 3485.

17. Medford AJ and Hatzell MC. Photon-driven nitrogen fixation: current progress, thermodynamic considerations, and future outlook. *ACS Catal* 2017; **7**: 2624–43.

18. Chen S, Perathoner S and Ampelli C *et al.* Electrocatalytic synthesis of ammonia at room temperature and atmospheric pressure from water and nitrogen on a carbon-nanotube-based electrocatalyst. *Angew Chem Int Ed* 2017; **56**: 2699–703.

19. Zhang N, Jalil A and Wu D *et al.* Refining defect states in $W_{18}O_{49}$ by Mo doping: a strategy for tuning N_2 activation towards solar-driven nitrogen fixation. *J Am Chem Soc* 2018; **140**: 9434–43.

20. Rosca V, Duca M and de Groot MT *et al.* Nitrogen cycle electrocatalysis. *Chem Rev* 2009; **109**: 2209–44.

21. Shi MM, Bao D and Wulan BR *et al.* Au sub-nanoclusters on TiO_2 toward highly efficient and selective electrocatalyst for N_2 conversion to NH_3 at ambient conditions. *Adv Mater* 2017; **29**: 1606550.

22. Pickett CJ and Talarmin J. Electrosynthesis of ammonia. *Nature* 1985; **317**: 652–3.

23. Bao D, Zhang Q and Meng FL *et al.* Electrochemical reduction of N_2 under ambient conditions for artificial N_2 fixation and renewable energy storage using N_2/NH_3 cycle. *Adv Mater* 2017; **29**: 1604799.

24. Zhou F, Azofra LM and Ali M *et al.* Electro-synthesis of ammonia from nitrogen at ambient temperature and pressure in ionic liquids. *Energy Environ Sci* 2017; **10**: 2516–20.

25. Showers WJ, Genna B and McDade T *et al.* Nitrate contamination in groundwater on an urbanized dairy farm. *Environ Sci Technol* 2008; **42**: 4683–8.

26. Castoldi L, Matarrese R and Morandi S *et al.* New insights on the adsorption, thermal decomposition and reduction of NO_x over Pt- and Ba-based catalysts. *Appl Catal B* 2018; **224**: 249–63.

27. Service RF. Liquid sunshine. *Science* 2018; **361**: 120–3.

28. APHA, AWWA, WPCF. *Standard Methods for the Examination of Water and Wastewater*. Washington, DC: American Public Health Association, 1998.

29. Duca M and Koper MTM. Powering denitrification: the perspectives of electro-catalytic nitrate reduction. *Energy Environ Sci* 2012; **5**: 9726–42.

30. Pérez-Gallent E, Figueiredo MC and Katsounaros I *et al.* Electrocatalytic reduction of nitrate on copper single crystals in acidic and alkaline solutions. *Electrochim Acta* 2017; **227**: 77–84.

31. Reyter D, Belanger D and Roue L. Nitrate removal by a paired electrolysis on copper and Ti/IrO$_2$ coupled electrodes-influence of the anode/cathode surface area ratio. *Water Res* 2010; **44**: 1918–26.

32. Dash BP and Chaudhari S. Electrochemical denitrificaton of simulated ground water. *Water Res* 2005; **39**: 4065–72.

33. Martinez-Huitle CA and Brillas E. Electrochemical alternatives for drinking water disinfection. *Angew Chem Int Ed* 2008; **47**: 1998–2005.

34. Martínez J, Ortiz A and Ortiz I. State-of-the-art and perspectives of the catalytic and electrocatalytic reduction of aqueous nitrates. *Appl Catal B* 2017; **207**: 42–59.

35. Ardenkjær-Larsen JH, Fridlund B and Gram A *et al.* Increase in signal-to-noise ratio of > 10,000 times in liquid-state NMR. *Proc Natl Acad Sci USA* 2003; **100**: 10158–63.

36. Perdew JP, Burke K and Ernzerhof M. Generalized gradient approximation made simple. *Phys Rev Lett* 1996; **77**: 3865–8.

37. Kresse G and Furthmüller J. Efficiency of ab-initio total energy calculations for metals and semiconductors using a plane-wave basis set. *Comput Mater Sci* 1996; **6**: 15–50.

38. Kresse G and Hafner J. Ab initio molecular dynamics for liquid metals. *Phys Rev B* 1993; **47**: 558–61.

39. Monkhorst HJ and Pack JD. Special points for Brillouin-zone integrations. *Phys Rev B* 1976; **13**: 5188–92.

40. Dion M, Rydberg H and Schröder E *et al.* Van der Waals density functional for general geometries. *Phys Rev Lett* 2004; **92**: 246401.

41. Klimeš J, Bowler DR and Michaelides A. Chemical accuracy for the van der Waals density functional. *J Phys Condens Matter* 2010; **22**: 022201.

42. Nørskov JK, Rossmeisl J and Logadottir A *et al.* Origin of the overpotential for oxygen reduction at a fuel-cell cathode. *J Phys Chem B* 2004; **108**: 17886–92.